Available online at www.sciencedirect.com
SCIENCE DIRECT®
Nuclear Physics A 732 (2004) 173–201
NUCLEAR PHYSICS A
www.elsevier.com/locate/npe

Isoscaling in central ^{124}Sn + ^{64}Ni, ^{112}Sn + ^{58}Ni collisions at 35 A MeV

E. Geraci [a,b], M. Bruno [a], M. D'Agostino [a,*], E. De Filippo [c], A. Pagano [c], G. Vannini [a], M. Alderighi [d], A. Anzalone [b], L. Auditore [e], V. Baran [b,f], R. Barnà [e], M. Bartolucci [g], I. Berceanu [f], J. Blicharska [h], A. Bonasera [b], B. Borderie [i], R. Bougault [j], J. Brzychczyk [k], G. Cardella [c], S. Cavallaro [b], A. Chbihi [l], J. Cibor [m], M. Colonna [b], D. De Pasquale [e], M. Di Toro [b], F. Giustolisi [c], A. Grzeszczuk [h], P. Guazzoni [g], D. Guinet [n], M. Iacono-Manno [b], A. Italiano [e], S. Kowalski [h], E. La Guidara [b], G. Lanzalone [b], G. Lanzanó [c], N. Le Neindre [i], S. Li [o], S. Lo Nigro [c], C. Maiolino [b], Z. Majka [k], G. Manfredi [g], T. Paduszynski [h], M. Papa [c], M. Petrovici [f], E. Piasecki [p], S. Pirrone [c], G. Politi [c], A. Pop [f], F. Porto [b], M.F. Rivet [i], E. Rosato [q], S. Russo [g], P. Russotto [b], G. Sechi [d], V. Simion [f], M.L. Sperduto [b], J.C. Steckmeyer [j], A. Trifirò [e], M. Trimarchi [e], M. Vigilante [q], J.P. Wieleczko [l], J. Wilczynski [r], H. Wu [o], Z. Xiao [o], L. Zetta [g], W. Zipper [h]

[a] *INFN, Sezione di Bologna, and Dipartimento di Fisica, Università di Bologna, Italy*
[b] *INFN, Laboratori Nazionali del Sud, and Dipartimento di Fisica e Astronomia, Università di Catania, Italy*
[c] *INFN, Sezione di Catania, and Dipartimento di Fisica e Astronomia, Università di Catania, Italy*
[d] *INFN, Sezione di Milano, and Istituto di Fisica Cosmica, CNR, Milano, Italy*
[e] *INFN, Gruppo Collegato di Messina, and Dipartimento di Fisica Università di Messina, Italy*
[f] *Institute for Physics and Nuclear Engineering, Bucharest, Romania*
[g] *INFN, Sezione di Milano, and Dipartimento di Fisica Università degli Studi, Milano, Italy*
[h] *Institute of Physics, University of Silesia, Katowice, Poland*
[i] *Institut de Physique Nucléaire, IN2P3-CNRS, Orsay, France*
[j] *LPC, ENSI Caen and Université de Caen, France*
[k] *M. Smoluchowski Institute of Physics, Jagellonian University, Cracow, Poland*
[l] *GANIL, CEA, IN2P3-CNRS, Caen, France*
[m] *H. Niewodniczanski Institute of Nuclear Physics, Cracov, Poland*
[n] *Institut de Physique Nucléaire, IN2P3-CNRS, Lyon, France*
[o] *Institute of Modern Physics, Lanzhou, China*
[p] *Institute of Experimental Physics, University of Warsaw, Poland*

0375-9474/$ – see front matter
doi:10.1016/j.nuclphysa.2003.11.055

[q] *INFN, Sezione di Napoli and Dipartimento di Fisica Università di Napoli, Napoli, Italy*
[r] *Institute for Nuclear Studies, Otwock-Swierk, Poland*

Received 23 July 2003; received in revised form 20 October 2003; accepted 24 November 2003

Abstract

$^{124}Sn + {}^{64}Ni$ and $^{112}Sn + {}^{58}Ni$ reactions at 35 A MeV incident energy were studied by using the 688 Si–CsI telescopes of the forward part ($1^\circ \leqslant \theta_{lab} \leqslant 30^\circ$) of CHIMERA multi-detector. The most central part, 1% of the total measured cross section was selected by means of a multidimensional analysis of the experimental observables. The detected isotopes of light fragments ($3 \leqslant Z \leqslant 8$) provided information on breakup temperatures of the emitting sources. The space–time structure of these sources was deduced from fragment correlations. An odd–even effect in the fragment production, enhanced by the isospin of the entrance channel, was observed. Freeze-out unbound neutron-to-proton relative densities for both studied reactions have been deduced, indicating for a possible isospin distillation mechanism related to a phenomenon of the liquid–gas phase transition in asymmetric systems.

PACS: 25.70.-z; 25.70.Pq; 24.10.Pa; 02.50.Sk

Keywords: NUCLEAR REACTIONS $^{112}Sn(^{58}Ni, X)$, $^{124}Sn(^{64}Ni, X)$, $E = 35$ A MeV; Nuclear fragmentation; Nuclear isospin; Heavy ion–nucleus reactions; Isotopes; Nuclear matter

1. Introduction

With the growing availability of radioactive beam facilities, the influence of the isospin degree of freedom on nuclear structure and reaction mechanisms has been strongly addressed. For a recent theoretical and experimental review on this field, see Ref. [1]. The ultimate goal is to have a better knowledge of the symmetry term of the nuclear equation of state (EOS). The density dependence of the symmetry term in EOS is poorly constrained by nuclear structure data. On the other hand, the symmetry term and its density dependence govern the density, radius and proton fraction of neutron stars and provide strong motivation for theoretical and experimental investigations.

For heavy systems, in which the neutron density exceeds the proton density, the symmetry term is repulsive for neutrons and attractive for protons. This therefore enhances the emission of neutrons relative to protons; the degree of enhancement reflects the magnitude of the symmetry term and its density dependence. The difference between neutron and proton emission rates can either be probed by direct measurements of pre-equilibrium neutrons and protons or by examining the isotopic composition of the bound fragments after fast emission [2–5].

* Corresponding author.
E-mail address: dagostino@bo.infn.it (M. D'Agostino).

Fragment observables for heavy ion reactions at intermediate energies (10 A MeV $\sim$ 100 A MeV) have been described successfully via either statistical [6–8] or dynamical [3, 9,10] models. Both of these calculations predict that the final isotopic composition of observed fragments should be sensitive to the density dependence of the symmetry term. To this end experimental information on the isotopic content of emitted fragments is a necessary starting point, together with the simultaneous measurements of quantities related to energy, emission angle, atomic number of a large fraction of the charged reaction products [11,12].

Very rich information has already been extracted from experimental studies on intermediate energy heavy ion collisions. Experiments have shown that the final state can be constrained to select the dynamics of the collision and isolate events that populate states which appear rather close to equilibrium [13–18]. Previous investigations have demonstrated that excited nuclear systems produced in such collisions undergo in a short breakup time scale (100 fm/c) [13,19–23] bulk multifragmentation characterized by production of several intermediate mass fragments ($Z \geqslant 3$). Decisive progress has been accomplished on the theoretical as well as on the experimental side in order to define and collect a converging ensemble of signals relating the multifragmentation to the nuclear liquid–gas phase transition [24] and to locate the position of this phenomenon in the phase diagram of nuclear matter [25].

Production yields of isotopically resolved nuclear particles and fragments not only can complete the knowledge of the EOS, by providing information on the N/Z degree of freedom, but also are essential in searching for possible occurrence of critical phenomena generated by fluctuations in the proton concentration of asymmetric nuclear matter [1].

Experimental isospin studies mostly rely on theoretical models based on the grand canonical ensemble (GCE) limit [1]. The detected light isotopes are treated as a diluted gas, under the basic assumption of thermal and chemical equilibrium. Moreover, the tools recently proposed [26–28] to get information on the free neutron and proton density proceed through ratios of isotope yields, produced in reactions differing only in the isospin asymmetry. This implies further assumptions on equality of temperatures and volumes of the emitting systems and on the cancellation of sequential feeding.

While it is well known from the literature how to safely measure the temperature of hot nuclear sources with "isotope thermometers", no studies have been done so far (to our knowledge) on the freeze-out space–time configuration through correlation functions of isotopically resolved fragments ($Z > 2$). Studies of this kind were only performed for isotopes of light charged particles [29–31] or neutrons [31].

Our purpose is therefore to fully characterize the emitting sources and verify all the hypotheses concerning these sources in the framework of GCE, prior to the analysis of the isotopic yields. In that way we aim to provide theoretical models [7,32] with robust set of data suitable to investigate the remaining problem of sequential feeding.

In this paper we present data concerning $^{124}\mathrm{Sn} + {}^{64}\mathrm{Ni}$ and $^{112}\mathrm{Sn} + {}^{58}\mathrm{Ni}$ central collisions at 35 A MeV. The measurements have been performed by using 688 Si–CsI telescopes of the forward part ($1^\circ \leqslant \theta_{\mathrm{lab}} \leqslant 30^\circ$) of CHIMERA apparatus [12] and beams from the Superconducting Cyclotron (CS) of the INFN Laboratori Nazionali del Sud in Catania.

We give a detailed analysis based on the asymptotic population of the reaction products represented by the experimentally detected isotopes. Particular attention is given to the

quantities characterizing the hot expanded sources emitting the observed fragments (such as their size, volume and temperature) for both studied reactions. We present different observations sensitive to the N/Z ratio of the system formed in the collisions. An "isoscaling analysis" for light isotopes (gas phase) is presented, aimed at observing a scaling behaviour, necessary condition for chemical equilibration. Moreover, ratios characterizing relative population of different pairs of isotopes enable us to extract the relative neutron to proton density for the two reactions, providing information on the phenomenon of isospin distillation.

In Section 2 a description of the experimental conditions is given; in Section 3 we briefly review the classical molecular dynamics (CMD) model and the statistical multifragmentation model (SMM). Calculations based on these models have been used in this paper, in order to have a check of the centrality selection and to characterize the excited sources formed in the most violent collisions. Section 4 describes the data selection through a principal component analysis (PCA) which reduces the number of observables characterizing the events. In Section 5 the emission patterns for the IMFs emitted in the measured reactions are discussed, together with the characteristics of the emitting sources. The isotope analysis is described in Section 6, and the conclusions are drawn in Section 7.

2. Experiment

Data from the ^{124}Sn + ^{64}Ni and ^{112}Sn + ^{58}Ni reactions, investigated at 35 A MeV incident energy of the beam from the Superconducting Cyclotron of LNS (Catania), have been collected by the Reverse collaboration [33,34].

The forward part ($1^\circ \leqslant \theta_{\rm lab} \leqslant 30^\circ$) of CHIMERA array [12] was used for the experiments. In this configuration, 688 telescopes made of ΔE silicon detectors 200–300 μm thick (depending on $\theta_{\rm lab}$) and CsI(Tl) stopping detectors were used.

The projectiles impinged on thin (200–300 μg/cm^2) self-supported Ni targets. The beam intensity was below 10^8 ion/s in order to keep the random coincidences as low as possible ($< 10^{-4}$). Events were registered when the silicon detectors of at least two telescopes ($M \geqslant 2$) were fired.

The energy resolution of silicon detectors and CsI(Tl) crystals was determined by measuring the elastic scattering of different ion beams, delivered by the Tandem and the Cyclotron accelerators of the LNS in Catania, impinging on a thin (~ 100 μg/cm^2) Au target. A typical energy resolution of a CHIMERA telescope was $< 1\%$ for silicon detectors and about 2% for CsI(Tl) crystals.

In order to identify the reaction products, several identification methods were used with this device [35]. The mass of the fragments stopped in the silicon detectors was extracted by using the time of flight technique. The light charged particles that punch through the silicon detector were identified applying the pulse shape method on the CsI(Tl) fast and slow components [36]. The ΔE–E method was applied to identify the charge of particles that punch through the silicon detectors.

Due to the very good performance of the apparatus, identification of the atomic numbers up to $Z = 50$ was achieved with a resolution better than one charge unit in the full dynamical range of the experiment.

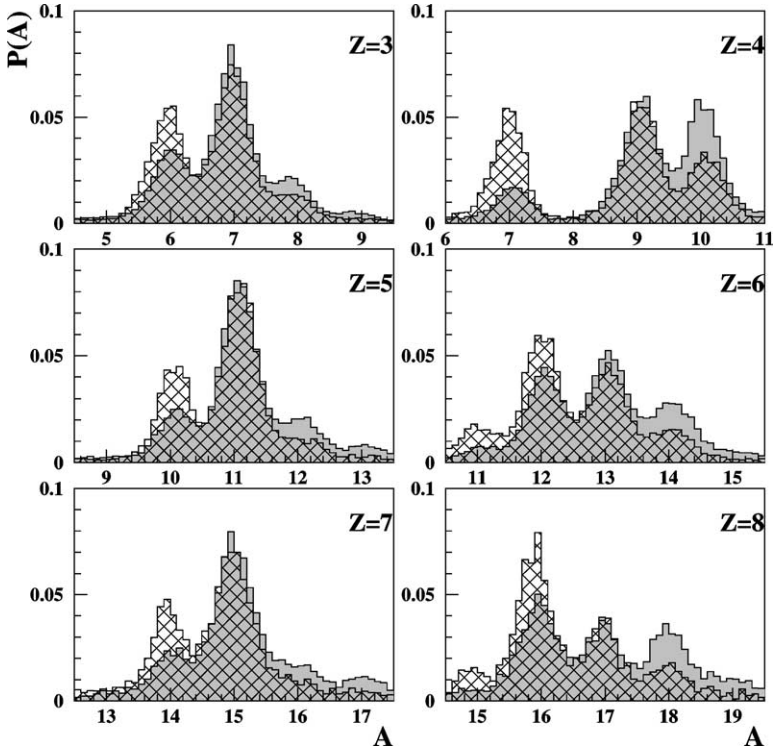

Fig. 1. Mass probability distribution of intermediate mass fragments ($3 \leqslant Z \leqslant 8$) for a telescope placed at 25° in the reactions ^{112}Sn + ^{58}Ni reaction (hatched histograms) and ^{124}Sn + ^{64}Ni reaction (grey histograms) at 35 A MeV.

An extension of this method [37] secured a good identification of isotopes in the angular range $\theta_{\text{lab}} = 13.5°$–30°. In the high gain conversion range of the QDC [12, 33], corresponding to a dynamical range of about 120 MeV with a sensitivity of the pre-amplifier of 4.5 mV/MeV, mass numbers were identified for fragments of charge $3 \leqslant Z \leqslant 8$, for energies larger than 3 (6) A MeV for $Z = 3$ (8).

In Fig. 1 we show the mass distribution for a telescope placed at 25°, for both studied reactions. The yields obtained with the method of Ref. [37] resulted in good agreement with those obtained with graphical cuts performed on the A-lines and with Gaussian integrals of the isotope distribution.

In this paper we report the results obtained from the analysis of IMFs ($Z \geqslant 3$). Light charged particles identified by the fast and slow signals of the CsI and charged products identified through their time-of-flight are only used to define the charged particle multiplicity. As deduced from simulations performed with the CMD [38] and SMM [7] models, the efficiency of the apparatus for the complete recording of the products of central collisions in reverse-kinematics reactions is larger than 95%.

3. Brief description of models used in data analysis

3.1. The CMD model

It is assumed in the CMD model [38] that in nucleus–nucleus collisions nucleons interact via a two body potential V composed of two different interactions [39]: the first one, for identical nucleons, is purely repulsive so no bound state of identical nucleons can exist (to mimic in some sense the Pauli principle), and the second, for proton neutron interaction, is attractive at large distances and repulsive at small ones. This potential gives an EOS of classical matter having about 250 MeV of compressibility. The EOS strikingly resembles that of nuclear matter (i.e., equilibrium density $\rho_0 = 0.16$ fm^{-3} and energy $E(\rho_0) = 16$ MeV/nucleon).

Both nuclei are initialized in their ground state by using the frictional cooling method [40], then they are boosted towards each other. Energy, linear and angular momentum, mass and charge numbers are conserved. In Refs. [39,41,42] it is shown that many experimental data on heavy ion collisions are reasonably explained by this classical model. However, even though this model takes into account all order correlations at the classical level, and this is quite important when studying instabilities, one has to remember that the classical structure of the model leads to an explosive behaviour at small impact parameters, concerning the amount of emitted fragments. Therefore, the analyses performed on CMD events can provide very useful, but mainly qualitative information and will be used in the following as a check of our centrality selection method.

3.2. The statistical multifragmentation model SMM

The statistical multifragmentation model SMM is based on the assumption of statistical equilibrium at a low density freeze-out stage of the nuclear system formed during the collision. At this stage, primary fragments are formed according to their equilibrium partitions.

Equilibrium partitions are calculated according to the microcanonical ensemble of all break-up channels composed of nucleons and excited fragments of different masses. The model conserves energy, momentum, mass and charge numbers.

The statistical weight of decay channel j is proportional to $\exp[S_j(E_s, V_s, A_s, Z_s)]$, where S_j is the entropy of the system in channel j and E_s, V_s, A_s and Z_s are the excitation energy, volume, mass and charge numbers of the fragmenting source.

Different breakup configurations are initialized according to their statistical weights. The fragments are then propagated in their mutual Coulomb field and allowed to undergo secondary decay. Light fragments with mass number $A \leqslant 4$ are considered as stable particles with only translational degrees of freedom; fragments with $A > 4$ are treated as heated nuclear liquid drops. The secondary decay of large fragments ($A > 16$) is calculated from an evaporation fission model, and that of smaller fragments from a Fermi breakup model [7].

The SMM model has already been shown to reproduce the main features of experimental systems close to the present one (see, for instance, Refs. [13,15,43–45]).

4. Event selection, central collisions

Several different methods have been used in order to select multifragmentation events in central heavy ions collisions [15,46–54]. These methods are mostly based on sorting the measured events as a function of one global observable (for instance, the multiplicity of the charged decay products [48] or their transverse energy [49,53,54]) correlated to the impact parameter of the reaction. In other methods [15,46,50] the events are sorted as a function of observables related to the shape of the event, like the sphericity and the coplanarity [46].

4π arrays make possible to handle, event by event, a large number of observables which can be used to characterize the event [55]. Thus, each event can be interpreted as a point in the multidimensional space given by all the measurable static and dynamic observables and their successive moments. Many kinds of multivariate analyses [56] can be employed to sort events and some of them have been already used successfully in heavy-ion induced reactions [18,43,57,58].

We applied to the data the principal component analysis (PCA), which determines the so-called principal variables, linear combinations of the primary global physical variables. The goal of PCA is to condense information into a minimum number of variables, since correlations among observables (like for instance the multiplicity and the transverse energy) are taken into account [43,57,58].

We analyzed several global observables through the PCA. Some of them are related to the centrality of the reaction, as for example, the light charged particle multiplicity N_{LCP}, the intermediate mass fragments ($Z \geqslant 3$) multiplicity N_{IMF}, the transverse energy E_{T} and the flow angle Θ_{flow} [46], i.e., the angle formed by the main eigenvector resulting from the event shape analysis and the beam axis. Other observables, like the size of the largest fragment Z_1 and the second moment of the charge distribution m_2 are related to the event charge partition. Finally other observables (the total detected charge Z_{Tot}, the total parallel momentum P_{ZTot} and the average velocity of the detected fragments along the beam direction V_{zfrag}) are connected to the efficiency of the experimental device for the measured reaction.

The events are plugged into a n-dimensional Hilbert space, where each axis of the basis corresponds to an observable variable. In order to make variables comparable and to get rid of the units, each variable X is firstly standardized (centered and reduced), i.e., replaced by $X' = (X - \langle X \rangle)/\sigma(X)$, where $\langle X \rangle$ is the mean value of X and $\sigma(X)$ its standard deviation. The cosine of the angle between any two axes is equal to the correlation coefficient of the two corresponding variables. Hence, if two variables are linearly correlated, their axes are superimposed. In this space, each event is represented by a point whose coordinates are equal to the values taken by the corresponding primary variables. The experimental events form a cloud whose center of mass is placed in the origin of the coordinate frame, due to the centering of the variables.

The covariance matrix of the global variables is built and diagonalized, to obtain the eigenvalues and the associated eigenvectors. The eigenvalues give the statistical information carried by the associated eigenvectors. When eigenvectors, linear combinations of the observable axes, are ordered with respect to the information they yield, principal components are defined. In the space defined by the principal components, events having the

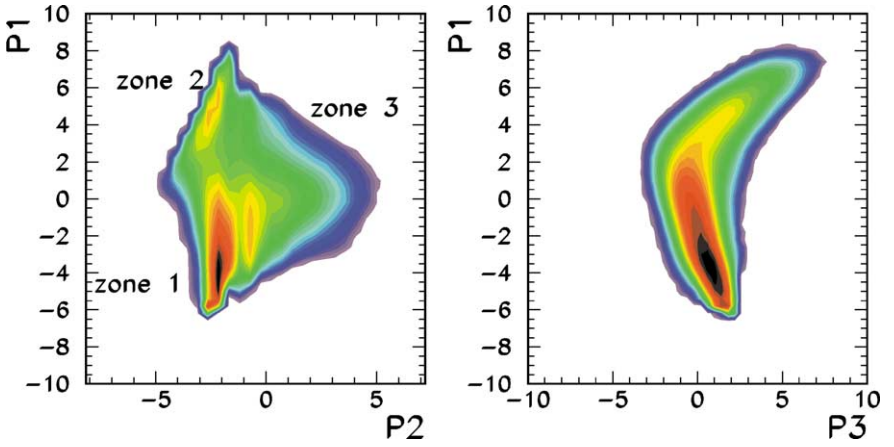

Fig. 2. Scatter plot of the measured events for the reaction ^{112}Sn + ^{58}Ni at 35 A MeV in the planes P1–P2 (left) and P1–P3 (right). P1, P2 and P3 are the first three principal components, carrying 80% of the original information. Black, red, yellow, green and blue denote sequence of decreasing yields.

same features (i.e., similar values of global variables) are grouped together, so defining in a natural way and without any previous selection, event classes.

As in Ref. [18], we found that about 80% of the original information contained in the global observables, listed above, is retained by the first three principal components. In particular, the percentage of information carried by P1, P2 and P3 is 0.52, 0.18 and 0.09, respectively. Therefore, in the following, we will analyze data in the 3-dimensional space defined by the three principal components, where the data exhaust most of the information.

In Fig. 2 we show the measured events projected on the P1–P2 (left panel) and P1–P3 (right panel) planes, while in Fig. 3 some experimental distributions corresponding to selected regions shown in Fig. 1 are displayed and hereafter commented.

Three distinct clouds of events are apparent in the left panel of Fig. 2. Two bumps, located at nearly constant values of P2 (P2 ≈ -2.5) correspond to events with low fragment multiplicity. The lower region, corresponding to the most negative values of P1 and P2 < 0 (Zone 1), contains almost completely detected events with high values of the total parallel momentum and the detected charge. Events belonging to this region are characterized by the U-shaped charge distribution. Therefore, these events can be associated with peripheral collisions. The cloud corresponding to P2 < 0 and positive values of P1 (Zone 2) contains poorly detected events made of few relatively light products. The region corresponding to high (and positive) values of P2 mostly contains well detected events, with high values of the IMF multiplicity. For P2 > 2 (Zone 3) the IMF multiplicity shows a peak at 3.5 and extends up to 8, and the charge distribution shows a monotonic decrease as a function of the fragment charge.

Information resulting from Figs. 2 and 3 can be summarized in the so-called *correlation plot*, discussed in Ref. [57]. Such a plot explains how the experimental observables are shared out in the principal planes. In Fig. 4 we show the correlation plots for the P1–P2 plane in the left panel and P1–P3 in the right one. The observables with projection close to the correlation circle are correlated most with the principal components, while observables

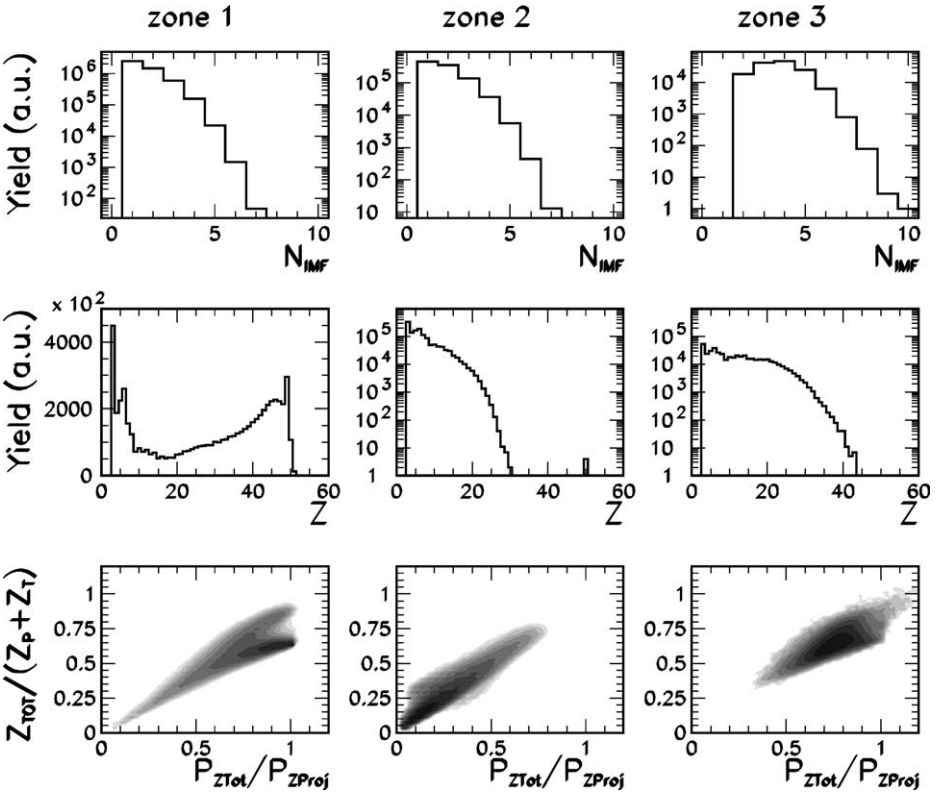

Fig. 3. Rows, from top to bottom: IMF multiplicity, charge distribution and scatter plot of the total detected charge versus the total detected parallel momentum. Columns: Zone 1, 2, 3 of Fig. 2 (see text). Darker shades represent larger cross sections.

with small projection (nearly orthogonal to the principal plane) give negligible contribution to the determination of these principal components.

From Fig. 4 (left panel) we see that the projection of observables related to the detector efficiency (Z_{Tot}, P_{ZTot}) are correlated to negative values of P_1 and positive values of P_2, while they do not contribute to P_3. The fragment multiplicity N_{IMF} is mainly correlated to P_2, as pointed out when discussing the panels of Fig. 3. In this representation also correlations/anticorrelations among experimental observables are apparent. The transverse energy E_{T} is correlated to the light charged particle multiplicity N_{LCP} and anticorrelated with $\cos(\Theta_{\mathrm{flow}})$. Indeed, central (peripheral) events are characterized by high (low) values of E_{T} and N_{LCP}, but low (high) values of $\cos(\Theta_{\mathrm{flow}})$.

We would like to express, however, caution concerning the use of the PCA. The correlation plot is rather specific for a given sample, because correlations among measured observables depend not only on physical processes, but also on the detector response. By analyzing model events, it was shown in Ref. [57] that the correlation plots before and after the filter are different, as they correspond to different samples of events and to different correlations among primary observables. For instance, suppose that the charge

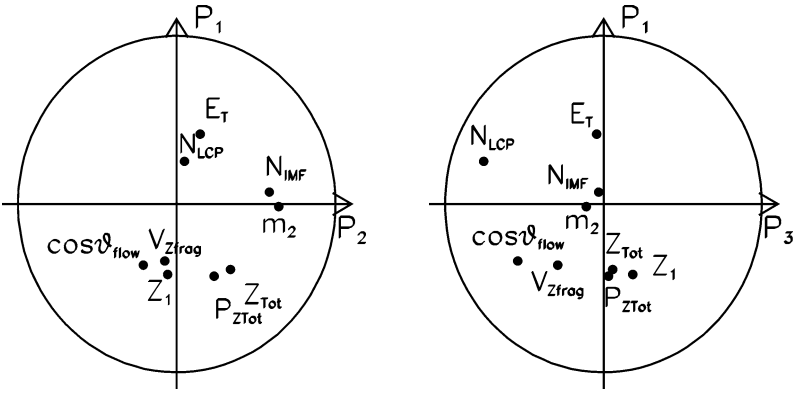

Fig. 4. Projection of the observables on the principal planes.

of the largest fragment, that physically is correlated to the impact parameter, strongly contributes to the determination of one of the principal components. This strong correlation may be washed out, however, after filtering the events, when the experimental device is not suitable to detect the largest charged fragment with high efficiency. Indeed, in many events the heaviest fragment is lost and only the second or third heaviest fragment is detected. The right correlation with the impact parameter is then recovered, thanks to constraints characterizing all the events applied to the analyzed sample.

Coming back to the analysis of our experimental sample, we have shown that Zone 3 of Fig. 2 is characterized by a high IMF multiplicity. Even though this region certainly contains multifragmentation events, a more careful selection has to be performed to separate central and semi-peripheral events.

In particular we look for a selection that would give an isotropic distribution of $\cos(\Theta_{\text{flow}})$, where Θ_{flow} results from an analysis of fragments' momenta in the centre of mass reference frame. A flat distribution of this observable, indeed, is typical of a fully equilibrated single source emission.

For well detected events in Zone 3 (where on the average 70% of the incoming total charge has been measured) we looked at the correlation between $\cos(\Theta_{\text{flow}})$ and the angle $\alpha = \text{arctg}(\text{P1}/\text{P3})$ which is a coordinate summarizing both the information provided by P1 and P3. This observable takes into account the position of each event in the P1–P3 plane. From Fig. 5 it is apparent that outside the region $120° < \alpha < 340°$ the events show a nearly flat (isotropic) distribution of $\cos(\Theta_{\text{flow}})$.

For matter of comparison, we present in the lower panels of Fig. 5 the charge asymmetry of the three heaviest charged products in each event [14], defined as:

$$a_{123} = \frac{\sqrt{(Z_1 - \langle Z\rangle)^2 + (Z_2 - \langle Z\rangle)^2 + (Z_3 - \langle Z\rangle)^2}}{\sqrt{6}\,\langle Z\rangle},$$

where $\langle Z\rangle = (Z_1 + Z_2 + Z_3)/3$. This observable ranges from 0 to 1. Symmetric charge partitions give $a_{123} = 0$, whereas events with two big fragments, nearly equal in size,

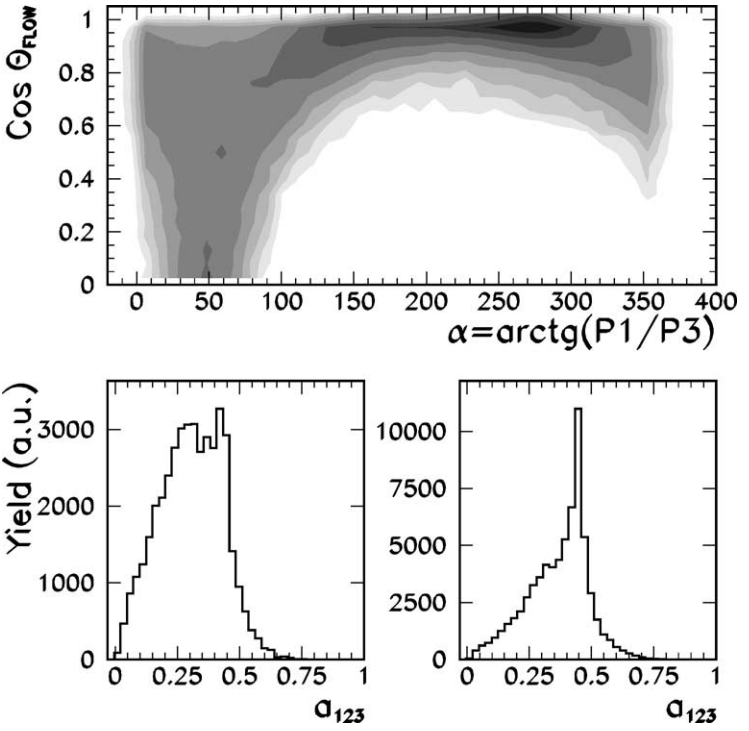

Fig. 5. Upper panel: contour plot of the correlation $\cos(\Theta_{\text{flow}})$ versus $\alpha = \text{arctg}(\text{P1}/\text{P3})$. Darker shades represent increasing cross sections (in the logarithmic scale). Lower panels: charge asymmetry of three heaviest fragments in each event. Left: $\alpha \leqslant 120^\circ$ or $\alpha \geqslant 340^\circ$, right: $120^\circ < \alpha < 340^\circ$.

accompanied by a small IMF should give $a_{123} = 0.5$ and events with only one very big fragment give $a_{123} = 1$.

Experimentally, events with a flat distribution of $\cos(\Theta_{\text{flow}})$ correspond to the more symmetric charge partitions (left lower panel of Fig. 5). The remaining events ($120^\circ < \alpha < 340^\circ$), showing $\cos(\Theta_{\text{flow}})$ forward peaked and an average asymmetry about 0.5, are characterized by two big fragments, similar in size. Therefore, they should correspond to symmetric fission events.

For the analysis hereafter presented we retained the class of central ($\alpha \leqslant 120^\circ$ or $\alpha \geqslant 340^\circ$) and well-detected events, approximately representing 1% of the total measured cross section.

It is interesting to apply the PCA to events generated by the CMD model, when the impact parameter is known event by event. To perform the PCA on CMD events, we took the same global observables as for data. The impact parameter (not used in the PCA) was then used to check the sorting of events by the principal components and thus the capability of PCA to provide information on the centrality of the reaction was tested. The PCA was performed on CMD events both before and after the experimental filter. The first 3 principal components encompass 80% of the global information.

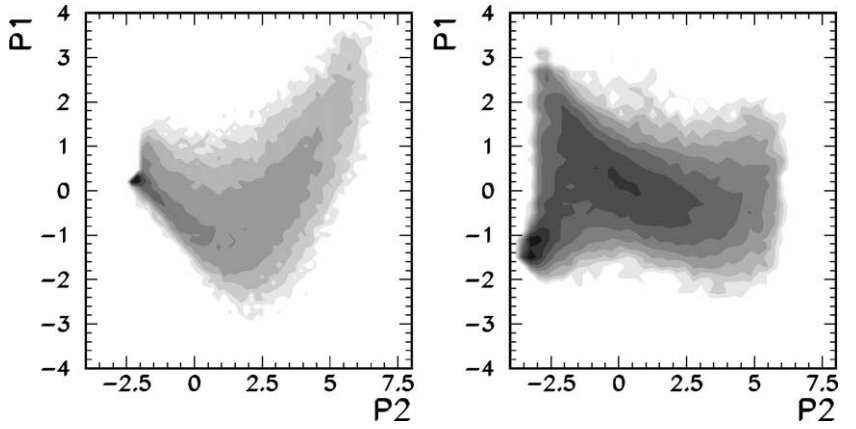

Fig. 6. Scatter plot of CMD events for the reaction $^{112}\mathrm{Sn} + {}^{58}\mathrm{Ni}$ at 35 A MeV in the plane P1–P2, before (left) and after (right) the filter. Grey scale is darker with increasing cross section.

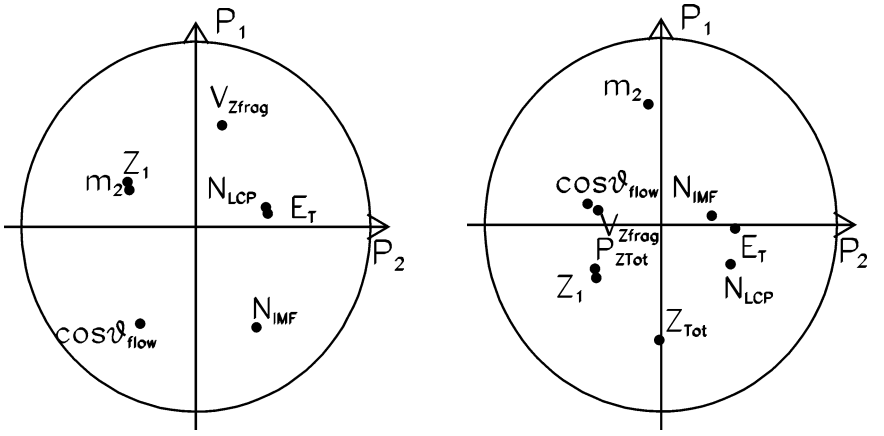

Fig. 7. CMD events: Projection on the principal plane P1–P2 of the observables, before (left) and after (right) the filter.

In Fig. 6 the scatter plot of CMD events in the plane defined by the first two principal components is presented. For not filtered events (left panel) only two distinct regions appear. When analyzing CMD events, after the geometrical efficiency and energy thresholds for charge identification being accounted for (right panel of Fig. 6), a third cloud of poorly detected events (similar to the experimental Zone 2 of Fig. 2) appears at high values of P1.

Also for these analyses we show the *correlation circle* before and after the filter (left and right panels of Fig. 8, respectively). As discussed above, the projections of some observables change after the filter, because correlations between experimental observables and true physical processes are modified by experimental conditions. However, in both

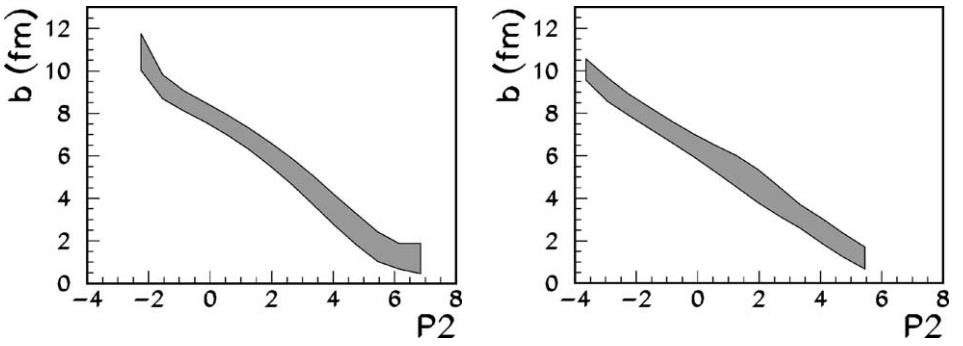

Fig. 8. CMD events for the reaction ^{112}Sn + ^{58}Ni at 35 A MeV: average value of the impact parameter b ± its standard deviation in bins of P2. Left (right) panel corresponds to CMD events before (after) the filter.

cases, the most negative values of P_2 correspond to peripheral collisions (high values of $\cos(\theta_{\text{flow}})$), while the events located at high and positive values of P2 correspond to central collisions. Indeed, the latter are characterized by large values of the charged-particle multiplicity N_{LCP}, fragment multiplicity N_{IMF}, and transverse energy E_{T}, and at the same time small values of $\cos(\theta_{\text{flow}})$.

In Fig. 8 we show the correlation between P2 and the impact parameter, before (left panel) and after (right panel) the software replica of the apparatus. In both cases the correlation is nearly linear and the standard deviation of the impact parameters, contributing to each bin of P2, does not exceed 0.7 fm (0.9 fm for the largest impact parameter $b = 10$–11 fm). We therefore interpret this analysis on CMD model events as a signal of a good data selection through PCA, even if the observables are spread by effects of the experimental efficiency and resolution.

5. Source characterization

5.1. Enhanced production of even-Z fragments

In Fig. 9 we compare the fragment charge distributions measured in central n-rich and n-poor reactions. The two distributions have been normalized to the number of events, i.e., $N(Z) = \text{Yield}(Z)/N_{\text{events}}$ and therefore represent the multiplicity of a given Z.

The integration of the reported distributions gives the IMF multiplicities. It results that they are approximately 10–20% larger for the ^{124}Sn + ^{64}Ni reaction than for the ^{112}Sn + ^{58}Ni one, consistent with previous experimental observations for symmetric Sn projectiles and targets [59] and BNV predictions [60].

For both reactions an enhancement in the production of even-to-odd-Z fragments is apparent. The enhancement is larger for the neutron poor reaction in comparison with the neutron rich one. This effect can be emphasized by looking at the ratio of the charge distribution of the neutron-poor reaction by the neutron-rich one (lower panel).

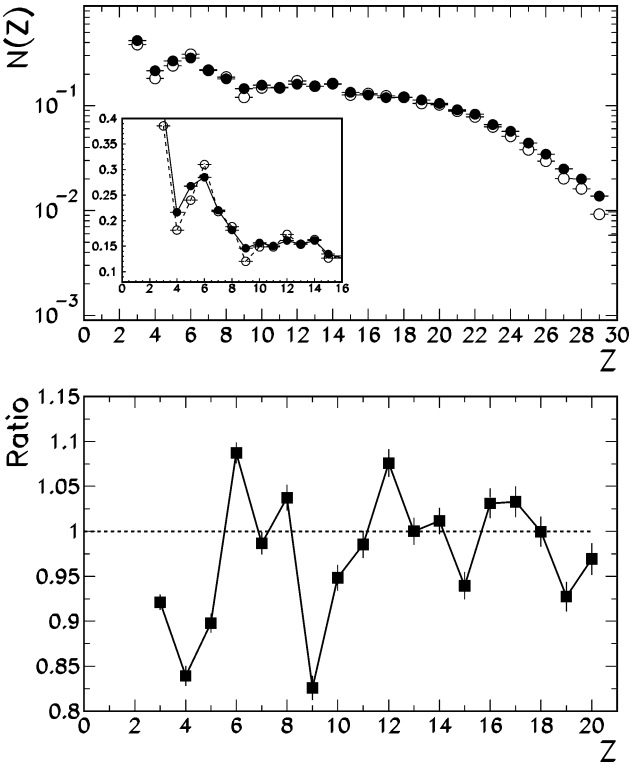

Fig. 9. Top panel: fragments ($Z \geqslant 3$) charge distribution for ^{112}Sn + ^{58}Ni (circles) and ^{124}Sn + ^{64}Ni (full symbols) systems. In the inserted panel a zoomed distribution is shown in linear scale. Bottom panel: ratio of the two distributions.

Odd–even effects in fragment charge distributions were observed in a variety of nuclear reactions with different dissipation, such as fission process [61,62] or heavy ion fragmentation reactions [63–66]. A possible explanation of this odd–even effect has been given in Ref. [67]. It seems to be related to the larger number of relatively stable isotopes of even-Z fragments in comparison to the odd-Z ones. This increases the probability to produce an even fragment rather than an odd one. In particular, from Table I of Ref. [67] it is evident that elements with odd-Z have fewer stable isotopes with lower N/Z values than even-Z elements. Most of odd-Z neutron poor stable isotopes generally have higher values of N/Z than neighboring even-Z nuclei.

Moreover, as already observed [68,69], a neutron-poor system will preferentially form neutron-poor isotopes, inducing an enhancement of even-Z element yields, which have more neutron-poor isotopes, and thus producing the observed odd–even effect. On the other hand, a neutron-rich system has the tendency to produce neutron-rich isotopes, which are equally abundant for even and odd-Z elements, weakening the odd–even effect.

The average N/Z ratio for fragments and its variance, shown in Fig. 10, also display an odd–even effect [70]. Accordingly with Ref. [67], fragments with an even-Z can have lower $\langle N/Z \rangle$, because more isotopes are available with low N/Z values. Consequently,

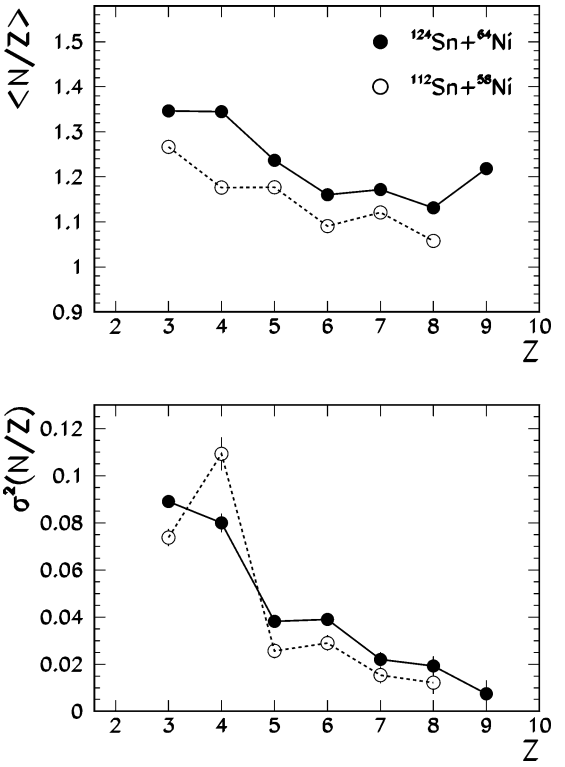

Fig. 10. Top panel: average neutron to proton ratio. Bottom panel: variance of mass distribution for light fragments ($Z = 3$–8). Symbols as in Fig. 9.

for these fragments, variances are higher. In addition, the beryllium's greater sensitivity to the N/Z of the compound system may be partially explained by the absence of ^{8}Be as a stable nucleus.

The higher number of available isotopes is reflected into a wider mass distribution for the even-Z fragments in comparison to the odd-Z ones, as deduced by the lower panel of Fig. 10, by taking into account that $\sigma^2(A) = Z^2\sigma^2(N/Z)$.

The enhancement in production of even relative to odd-Z elements from intermediate energy heavy ion collisions is therefore due to the availability of isotopes with relatively high binding energies. This experimental observation should be taken into account in dynamical [60,71] and statistical studies aimed at determining the freeze-out composition of excited systems formed in heavy ion collisions.

5.2. Source size and excitation energy

To get information on the characteristics of the source, formed in central collisions and generating the decay products asymptotically detected, and in order to assess its thermal equilibrium, we performed a comparison between data and statistical model (SMM [7]) predictions. The simulated events were filtered, by taking into account the geometrical

efficiency and the energy threshold for charge identification. The same normalization to the total number of events was then applied to the experimental and calculated distributions, enabling the comparison in the absolute scale.

The input parameters for the statistical model (size and excitation energy of the source) were chosen in agreement with the predictions of the dynamical model BNV [4,5,72]. For an impact parameter $b = 1$ fm this model predicts that for the n-poor (rich) reaction a thermally equilibrated excited system is formed 120 fm/c after the collision. The mass of the system is $A = 153$ (169), the charge $Z = 69$ (70), the thermal excitation energy $E^*/A = 5.4$ (5.3) MeV.

It is interesting to report the prediction of the BNV calculation for the pre-equilibrium stage. On the average, the neutron poor system, after 120 fm/c from the collision, emits 9 protons and 8 neutrons. This fixes the N/Z ratio of the equilibrated remaining source to 1.22. This value shows an enrichment in protons as compared to stable nuclei of the same mass ($N/Z = 1.4$), but is close to the initial value of N/Z of the system, $N/Z = 1.18$.

As far as the neutron-rich system is concerned, before the equilibration time, the pre-equilibrium emission gives 8 protons and 11 neutrons, so that the N/Z of the equilibrated emitting source is 1.41, again equal to that of the system.

For the same impact parameter, the CHIMERA code [73], a microscopic model based on the concept of molecular dynamics that simulates some quantum effects enabling studies of large fermionic systems, predicts a minimum of the density for the n-poor (rich) reaction of $\rho/\rho_0 = 0.38$ (0.37). The resulting mass of the thermalized system is $A = 139$ (155), and charge $Z = 64$ (67), so that $N/Z = 1.18$ (1.33).

As far as SMM predictions are concerned, we found a close reproduction of the experimental observables by the statistical model, provided that a source for the n-poor reaction is assumed to have mass $A = 145$ and charge $Z = 66$. For the neutron rich reaction, the mass of the source needs to be increased to $A = 160$. As far as the excitation energy is concerned, in both cases the best agreement between data and model predictions is achieved for an excitation energy about 5 A MeV. For the freeze-out volume in the model we have taken the usual value of $3V_0$. The small deviations of the SMM inputs with respect to BNV and CHIMERA predictions can be understood taking into account that in dynamical models, source characteristics depend on the time during the evaporation process.

The comparison between measured observables and model predictions is presented in Figs. 11 and 12. For sake of simplicity we report only results for the n-poor reaction. For the n-rich reaction, the agreement is equally good.

Not only low-order mean moments of the charge distributions are reproduced (i.e., average multiplicities of light charged particles and fragments, see Fig. 11), but also their distributions. In addition, the comparison of the charge distribution of three heaviest fragments in each event (Fig. 12) allowed us to check the model predictions of the charge partition.

Also for kinetic observables (lower panels in Fig. 11) the agreement between data and model is quite good. Even though some small distortions can be observed in the angular distribution, an advanced stage of equilibration is apparent in the experimentally selected set of events.

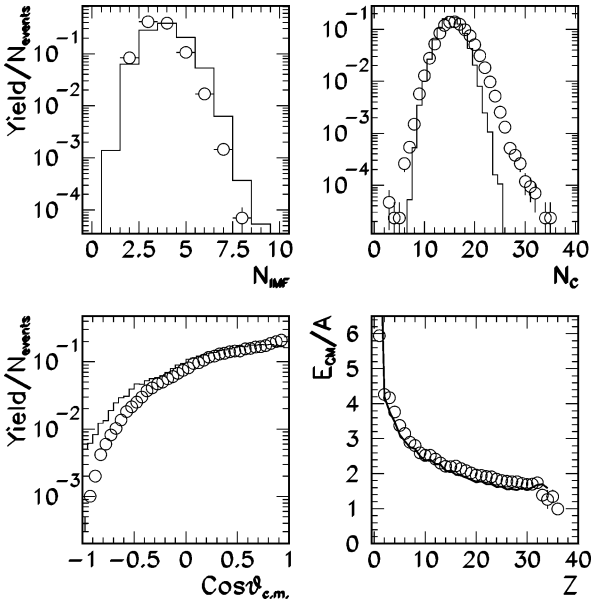

Fig. 11. IMF multiplicity, total-charged particle multiplicity, fragments $\cos(\theta_{\mathrm{c.m.}})$ distribution, and mean kinetic energy per nucleon in the CM reference frame as a function of the fragment charge. Circles represent data, lines show SMM-filtered predictions for central $^{112}\mathrm{Sn} + {}^{58}\mathrm{Ni}$ collisions.

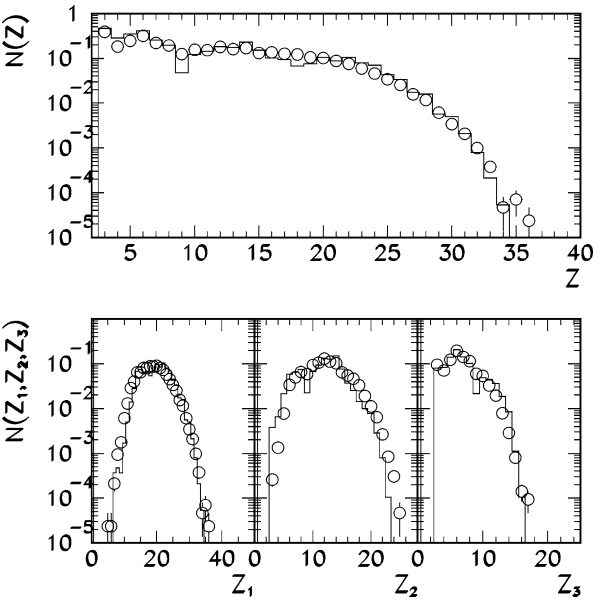

Fig. 12. Charge distribution and charge partition, i.e., charge distributions of the heaviest three fragments in each event ($Z_1 \geqslant Z_2 \geqslant Z_3$). Circles represent data, lines show SMM-filtered predictions for central $^{112}\mathrm{Sn} + {}^{58}\mathrm{Ni}$ collisions.

It would be interesting to carry out similar calculations with stochastic dynamical models [17,74], but more work has still to be done in this direction.

5.3. Space–time configuration: isotope correlations functions

Information about the space–time evolution of the reaction zone can be obtained via correlation functions. The principle behind such technique is similar to the intensity interferometry [75] employed to determine the radius of stars, where both singles and coincident yields of photons from the same source (star) are measured. In nuclear physics, particles are detected instead of photons. Unlike in astronomy, where the space–time evolution of stars is slow, the time scale involved in nuclear processes is very short. Thus there could be ambiguities in determining the size and time-scale of hot nuclear systems using correlation functions, because a small source emitting over a long period of time behaves like a large source emitting over a short period of time [76].

In the present work we do not attempt to analyze in detail the space–time information of the emitting sources by comparing data with many-body trajectory calculations [13,19–23, 77]. Instead, we would like only to check whether the sources formed in central collisions for both studied reactions show the same behaviour for isotopically identified fragments ($3 \leqslant Z \leqslant 8$). To verify this question we calculated the velocity correlation function for every pair of fragments as:

$$1 + R(v_{\mathrm{red}}) = C \frac{Y(v_{\mathrm{red}})}{Y_{\mathrm{back}}(v_{\mathrm{red}})} \tag{1}$$

where

$$v_{\mathrm{red}} = |(\vec{v}_i - \vec{v}_j)| \sqrt{\mu_{ij}/(2Z_iZ_j)} \tag{2}$$

is the reduced relative velocity of fragments i and j with atomic numbers Z_i and Z_j, and μ_{ij} is the reduced mass of that sub-system. Definition of this observable comes from the hypothesis that on the average the relative velocity of each pair of fragments originating from the same source is their relative velocity of mutual Coulomb repulsion. Assuming $A = 2Z$, v_{red} reduces to the commonly used expression

$$v_{\mathrm{red}} = \frac{|(\vec{v}_i - \vec{v}_j)|}{\sqrt{Z_i + Z_j}}.$$

By using v_{red}, one can jointly analyze pairs of fragments of different charges.

In Eq. (1), $Y(v_{\mathrm{red}})$ and $Y_{\mathrm{back}}(v_{\mathrm{red}})$ are the coincidence and background yields for fragment pairs of reduced velocity v_{red}. The background yield is constructed by means of the mixed event technique [78]. C is a normalization factor fixed by the requirement to have the same number of true and mixed pairs [79]. Although some other normalization prescriptions are also used, our basic qualitative conclusions are independent of the particular choice of normalization.

In Fig. 13 the correlation functions are shown for all fragments isotopically resolved ($3 \leqslant Z \leqslant 8$) from ^{6}Li to ^{18}O for both studied reactions. Reduced velocities were calculated with Eq.(2), without any simplifying assumptions, because mass numbers were identified for these fragments.

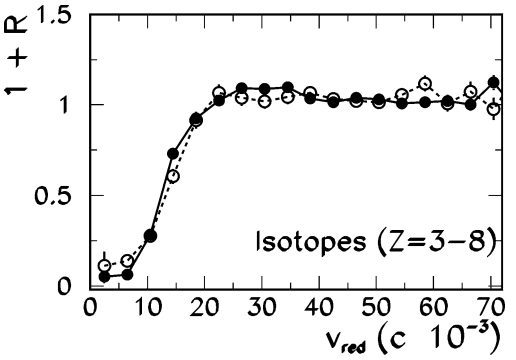

Fig. 13. Two-fragment correlation functions of the reduced velocity for isotopically resolved IMFs of $3 \leqslant Z \leqslant 8$ (from ^{6}Li to ^{18}O), for both studied reactions. Solid symbols (solid line) refer to ^{124}Sn + ^{64}Ni central collisions, open symbols (dashed line) to ^{112}Sn + ^{58}Ni central collisions. The lines are drawn to guide the eye.

From Fig. 13 it is clearly seen that the decay of sources formed in ^{112}Sn + ^{58}Ni and ^{124}Sn + ^{64}Ni central collisions leads to almost identical space–time emission patterns. Indeed, for both reactions the width of the "Coulomb hole", related to the size of the emitting source in space and time, looks almost identical.

It has been proven in Ref. [80] that correlation functions can also provide information on ordering of the fragments' emission. For instance, for events with light fragments mostly emitted in secondary de-excitation processes, the correlation functions should show narrower depletion at small reduced velocities than in case of emission of these products during all stages of the reaction.

As mentioned in the introduction, this point is quite important because we are going to study the isotopic observables in very detail. One of the open problems is the influence of the sequential feeding on these observables. It is obvious that a large secondary emission of light isotopes would prevent reliable calculations of the neutron-to-proton relative densities at the freeze-out configuration. We carried out tests by selecting from the set of events analyzed in Fig. 13 two subsets of events in which either light ^{7}Li or ^{10,11,12}B were selected as one fragment of the pair. In Fig. 14 we show the corresponding correlation functions, for both studied reactions (grey areas) and we compare them with the correlations already shown in Fig. 13, i.e., integrated over all the isotopic partitions (circles).

As seen from Fig. 14, the width of the "Coulomb hole" does not depend on the chosen decay configuration. This indicates that the size of the emitting sources in space and time are independent on specific isotopic partition. This conclusion holds for all other selections which we were able to test. As far as we know, this is the first time that the correlation functions were determined for isotopically resolved fragments, over a large fraction of the solid angle.

The correlation functions of the reduced velocity deserve further investigations [81]. Indeed, with this technique [30,82] one can try to evaluate the percentage of secondarily evaporated particles and the average excitation energy of primary fragments, an important detailed information on the freeze-out stage of the reaction.

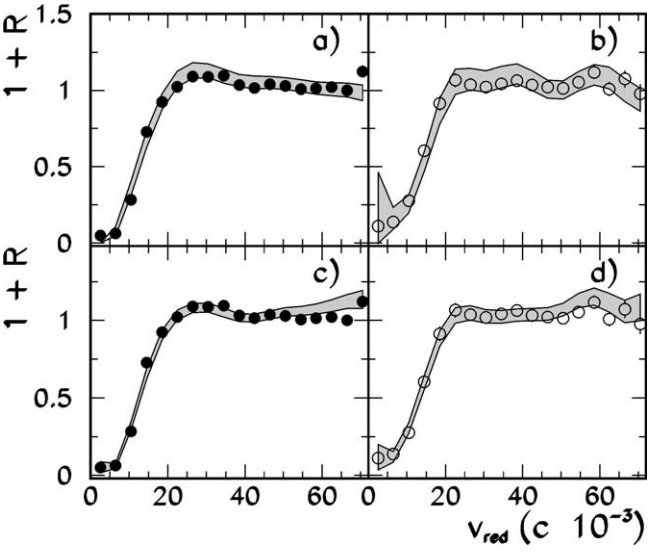

Fig. 14. Two-fragment correlation functions for subsets of events containing a ^{7}Li and a ^{10,11,12}B (grey areas in the upper and lower panels, respectively), compared to the results for the complete set of isotopes (circles), as on Fig. 13. Panels (a) and (c) refer to the ^{124}Sn + ^{64}Ni reaction, panels (b) and (d) to the ^{112}Sn + ^{58}Ni reaction.

6. Isotope analysis

We have shown in the previous section that the statistical model reasonably reproduces the charge distributions measured in the ^{124}Sn + ^{64}Ni and ^{112}Sn + ^{58}Ni reactions at nearly the same thermal excitation energy per nucleon. In this section we calculate the isotopic temperature for the two systems and perform a detailed analysis investigating for isospin distillation effects.

6.1. Source temperature

In the literature (see, for instance, Ref. [1]) the isotopic temperature analyses have been performed in the approximation of a dilute gas in the grand canonical ensemble limit with thermal and chemical equilibrium [83]. The starting point is the production of isotopes with N neutrons and Z protons, governed by the chemical potentials for the neutrons and protons in the system (or by the nucleon densities ρ_n, ρ_p), by the temperature T, and individual binding energies of various isotopes $B(N, Z)$,

$$\begin{aligned} Y(N,Z) &= F(N,Z,T)e^{B(N,Z)/T}e^{(N\mu_n+Z\mu_p)/T} \\ &= F(N,Z,T)\rho_n^N\rho_p^Z e^{B(N,Z)/T}. \end{aligned} \tag{3}$$

The factor $F(N, Z, T)$ includes the volume term and information about the secondary decay contributions from both particle-stable and unstable states to the final ground-state yields.

In the formula for calculating the isotope temperatures we make use of the ratio R:

$$R = \frac{Y(A_i, Z_i)/Y(A_i + 1, Z_i)}{Y(A_j, Z_j)/Y(A_j + 1, Z_j)}, \tag{4}$$

where values of Y are given by Eq. (3), calculated for the ground states. The temperature is given by:

$$T = \frac{B}{\ln(sR)}, \tag{5}$$

where B is related to binding energies and s to the ground state spins:

$$B = BE(A_i, Z_i) - BE(A_i + 1, Z_i) - BE(A_j, Z_j) + BE(A_j + 1, Z_j), \tag{6}$$

$$s = \frac{[2S(A_j, Z_j) + 1]/[2S(A_j + 1, Z_j) + 1]}{[2S(A_i, Z_i) + 1]/[2S(A_i + 1, Z_i) + 1]}. \tag{7}$$

The formula is exact (in the grand canonical model) if secondary decays, which could alter primary populations, are negligible. This assumption is rather problematic as the measured yields correspond to cold fragments containing contributions from the decays of many excited nuclei [84–86]. The change of yields due to secondary decays can cause Eq. (5) to give significantly different temperatures from the true grand canonical temperature. This question was studied in detail in Ref. [86]. It was shown that for large differences in the binding energy parameter $B > 10$ MeV, the difference between apparent temperature and the true grand canonical temperature decreases. This results suggests that in order to deduce the temperature from experimental data using Eq. (5) it is advisable to use pairs having a large value of B.

Measured yields of isotopes from lithium to oxygen were used to construct the temperature observables from double-isotope ratios [83] for the reactions studied in this experiment. All the isotopic thermometers fulfill the requirement that the double difference of the binding energies is larger than the anticipated temperatures [86,87]. Therefore, we presume that these isotopic thermometers are not strongly influenced by sequential decay. So-called apparent temperatures and temperatures obtained after correction as in Ref. [86], together with estimated statistical errors, are presented in Tables 1 and 2 for both studied reactions.

The deduced values of the temperature are in the range typical for reactions near the onset of multi-fragment emission [86–89]. Within statistical errors, the temperatures are equal for both reactions.

For the ^{112}Sn + ^{58}Ni reaction, the weighted average temperature before and after the correction is 3.31 ± 0.03 MeV and 3.96 ± 0.04 MeV, respectively. For the ^{124}Sn + ^{64}Ni reaction, these average values are 3.33 ± 0.03 MeV and 3.94 ± 0.03 MeV. It seems therefore reasonable to assume that sources formed in central collisions in both studied reactions have the same temperature. The temperatures before and after correction, obtained by averaging all results from Tables 1 and 2 are 3.32 ± 0.02 MeV and 3.95 ± 0.03 MeV, respectively.

Table 1
Apparent and corrected temperatures for the $^{112}Sn + {}^{58}Ni$ reaction

Thermometer	$T_{apparent}$ (MeV)	$T_{corrected}$ (MeV)
$^{6}Li/^{7}Li$–$^{11}C/^{12}C$	4.16 ± 0.12	3.58 ± 0.09
$^{7}Li/^{8}Li$–$^{11}C/^{12}C$	3.89 ± 0.08	4.46 ± 0.11
$^{9}Be/^{10}Be$–$^{11}C/^{12}C$	6.81 ± 0.39	4.09 ± 0.14
$^{11}B/^{12}B$–$^{11}C/^{12}C$	4.07 ± 0.11	4.24 ± 0.12
$^{11}C/^{12}C$–$^{12}C/^{13}C$	3.89 ± 0.10	3.91 ± 0.10
$^{11}C/^{12}C$–$^{13}C/^{14}C$	3.85 ± 0.14	4.19 ± 0.16
$^{15}O/^{16}O$–$^{16}O/^{17}O$	2.46 ± 0.07	3.83 ± 0.16
$^{11}C/^{12}C$–$^{16}O/^{17}O$	2.85 ± 0.06	3.73 ± 0.10

Table 2
Apparent and corrected temperatures for the $^{124}Sn + {}^{64}Ni$ reaction

Thermometer	$T_{apparent}$ (MeV)	$T_{corrected}$ (MeV)
$^{6}Li/^{7}Li$–$^{11}C/^{12}C$	4.11 ± 0.11	3.54 ± 0.08
$^{7}Li/^{8}Li$–$^{11}C/^{12}C$	3.69 ± 0.06	4.20 ± 0.08
$^{9}Be/^{10}Be$–$^{11}C/^{12}C$	6.73 ± 0.31	4.06 ± 0.11
$^{11}B/^{12}B$–$^{11}C/^{12}C$	4.03 ± 0.09	4.20 ± 0.09
$^{11}C/^{12}C$–$^{12}C/^{13}C$	3.87 ± 0.09	3.89 ± 0.09
$^{11}C/^{12}C$–$^{13}C/^{14}C$	3.72 ± 0.11	4.03 ± 0.13
$^{15}O/^{16}O$–$^{16}O/^{17}O$	2.56 ± 0.06	4.07 ± 0.16
$^{11}C/^{12}C$–$^{16}O/^{17}O$	2.85 ± 0.05	3.73 ± 0.09

6.2. Isoscaling analysis and isospin distillation

Isospin effects may significantly influence the liquid–gas phase transition in nuclei. As the asymmetry between neutron and proton densities becomes a local property in a given nuclear system, calculations predict neutrons and protons to be non homogeneously distributed within the system, resulting in formation of a relatively neutron-rich gas and relatively neutron-poor liquid [4,90–93]. This effect, quoted as isospin distillation, occurs in unstable asymmetric nuclear matter and consists in the migration towards high density domains more frequently by protons than neutrons, thus leading to the formation of more symmetric fragments (liquid phase) [94]. The critical temperature may decrease with increasing neutron excess reflecting the fact that a pure neutron liquid does not probably exist [90]. Recent calculations suggest that the rather narrow range of isospin values available in the laboratory experiments might not allow us to observe the decrease of the critical temperature [95]. Several projects are underway to study the distillation of the isospin in the co-existence region. As the isospin effects are not large, the influence of sequential decays may obscure the isospin effects that we would like to study.

Assuming a clear two-phase separation in the coexistence region, we can adopt an experimental method to directly determine the neutron enrichment of the gas phase which should be more pronounced in more asymmetric system. This approach is based on

measurements of the yield of light isotopes formed in the gas phase [26]. Considering the detected light isotopes (i.e., the asymptotic products) in the approximation of a dilute gas in the grand canonical ensemble limit with thermal and chemical equilibrium (Eq. (3)), it is possible to get information on the isospin distillation, as well as a coherent description of the thermodynamical coordinates of the emitting excited systems.

To do this and to bypass the sequential decay problem, observables involving ratios of the measured isotope yields are used. This method relies on extracting the relative neutron and proton densities from two similar reactions, which differ only in isospin. If one constructs the ratio of $Y(N, Z)$ (Eq. (3)) from two different reactions, the relative isotope ratio, $R_{21}(N, Z)$, has a simple dependence on the relative neutron and proton densities of the free nucleon gas:

$$R_{21}(N, Z) = \frac{Y_2(N, Z)}{Y_1(N, Z)} = Ce^{N\Delta\mu_n/T} e^{Z\Delta\mu_p/T} = C\left(\frac{\rho_{n,2}}{\rho_{n,1}}\right)^N \left(\frac{\rho_{p,2}}{\rho_{p,1}}\right)^Z = C\hat{\rho}_n^N \hat{\rho}_p^Z. \tag{8}$$

Here, C is an overall normalization factor and $\hat{\rho_n}$, $\hat{\rho_p}$ are the relative neutron and proton densities, related to the isoscaling parameters $\alpha = \Delta\mu_n/T$ and $\beta = \Delta\mu_p/T$ of Refs. [27, 28] by the relationships: $e^\alpha = \hat{\rho_n}$ and $e^\beta = \hat{\rho_p}$.

In the case when the system is more neutron-rich in reaction 2 than in reaction 1, one expects $\hat{\rho_n}$ to be larger than 1 ($\alpha > 0$) and $\hat{\rho_p}$ to be lower than 1 ($\beta < 0$).

To eliminate uncertainties in the normalization of the data sets measured for both studied reactions, we adopted the procedure of Ref. [28], introducing the reduced isotopic ratio for fragments X, normalized with respect to this ratio for ^{6}Li, i.e., $R_{21}(\mathrm{X})/R_{21}(^6\mathrm{Li})$.

The basic assumption for justifying Eq. (8) is that the sources formed in both studied reactions have the same volume and temperature. We have shown in previous sections that this assumption is well satisfied in our data.

We recall here that similarly as in Ref. [96], the fact of observation of approximately identical isotopic temperatures in the ^{112}Sn + ^{58}Ni and ^{124}Sn + ^{64}Ni reactions at 35 MeV per nucleon, is a feature of more general phenomenon of isoscaling. Indeed, this fact is a consequence of Eq. (8), according to which the double yield ratios (from which isotope temperatures are derived) are identical for both reactions.

Another important information on neutron and proton densities comes from mirror yield ratios. If the sequential decay and the Coulomb effects are small, the dependence of isobaric mirror yield ratios on the binding energy difference should be exponential, i.e., of the form:

$$(\rho_n/\rho_p)_i \exp(\Delta B/T_i), \tag{9}$$

where T_i is the temperature of the emitting source for the reaction i and $(\rho_n)_i$ and $(\rho_p)_i$ are the neutron and proton densities for this reaction. Therefore, the analysis of isotopic and mirror ratios enables one to extract simultaneously the relative densities $\hat{\rho_n}$ and $\hat{\rho_p}$ (i.e., the isoscaling parameters α, β) and the free neutron-to-proton density ratio ρ_n/ρ_p for each reaction.

A constrained fit of the isotopic ratios (20 points) measured for two reactions and of the isobar ratios (7 points) for mirror nuclei has been performed. The isotopic temperature

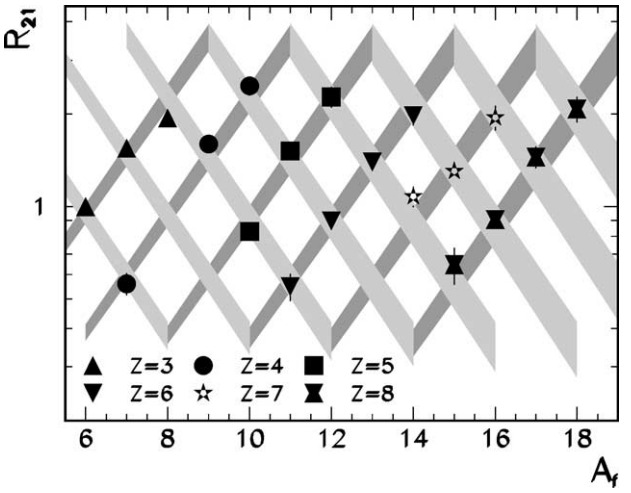

Fig. 15. Isotopic ratio R_{21}, normalized with respect to $R_{21}(^6\mathrm{Li})$, versus the mass number A_f of the detected fragment. Li, Be, B, C, N and O fragments are indicated by different symbols. The result of a four-parameter fit to the data with Eqs. (8) and (9) is represented by regions of constant charge (dark grey) and constant neutron number (light grey).

(discussed in the previous section) was assumed as the temperature of the emitting systems. The parameters of the fit are the relative neutron density $\rho_{n,2}/\rho_{n,1} = \hat{\rho_n}$, the relative proton density $\rho_{p,2}/\rho_{p,1} = \hat{\rho_p}$, the normalization constant C of Eq. (8), and the free neutron-to-proton density ratio for the reaction $^{124}\mathrm{Sn} + {}^{64}\mathrm{Ni}$, $(\rho_n/\rho_p)_{124}$. For the reaction $^{112}\mathrm{Sn} + {}^{58}\mathrm{Ni}$, the free neutron to proton density has been derived from Eqs. (8) and (9) as: $(\rho_n/\rho_p)_{112} = (\rho_n/\rho_p)_{124} \cdot \hat{\rho}_p/\hat{\rho}_n$.

The results of the fit are shown in Figs. 15 and 16. The experimentally determined ratios are indicated by different symbols. The grey areas represent predictions of Eqs. (8) and (9), corresponding to the values of the parameters within their errors.

Since it is not well established whether or not sequential feeding effects affect in the same way mirror ratios and the isotopic temperature, we performed the fit taking as the temperature the corrected isotopic temperature (light grey area in Fig. 16) or the uncorrected value (dark grey area in Fig. 16).

All the isotopic ratios follow the dependence of Eq. (8) very well while the experimental mirror ratios oscillate around the relationship of Eq. (9). Many versions of the statistical model, such as the grand canonical model [83,97] of multifragmentation, predict both the isoscaling and mirror-nuclei ratio dependence. The resulting fitting parameters are: $\hat{\rho_n} = 1.55 \pm 0.02$, $\hat{\rho_p} = 0.63 \pm 0.01$ and $C = 1.02 \pm 0.05$.

When the corrected isotopic temperature is used in the fit, the result is: $(\rho_n/\rho_p)_{124} = 6.5 \pm 0.2$ and $(\rho_n/\rho_p)_{112} = 2.6 \pm 0.1$. By using the apparent isotopic temperatures the result changes into: $(\rho_n/\rho_p)_{124} = 5.8 \pm 0.2$ and $(\rho_n/\rho_p)_{112} = 2.4 \pm 0.1$. The values of $\hat{\rho_n}$ and $\hat{\rho_p}$ lead to isoscaling parameters $\alpha = 0.44 \pm 0.01$ and $\beta = -0.46 \pm 0.02$, in agreement with the general trend discussed in Refs. [27] and [28]. It is worth mentioning that the value of α and β change with the freeze-out volume and the temperature of the source [98]. It is

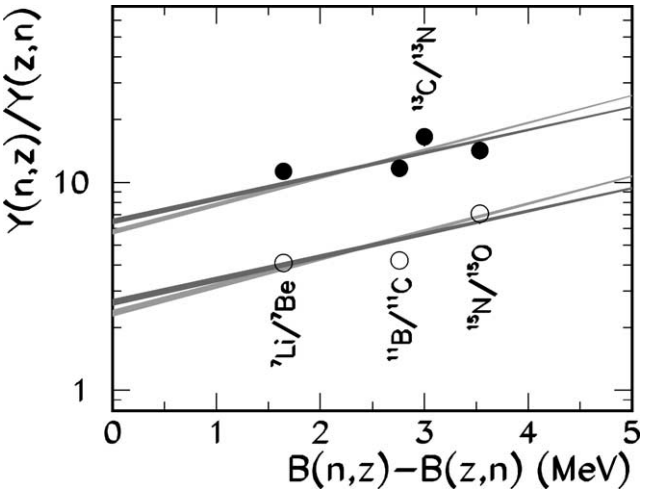

Fig. 16. Isobar ratios as a function of the binding energy difference ΔB for mirror nuclei obtained from the $^{112}\mathrm{Sn} + {}^{58}\mathrm{Ni}$ (open circles) and $^{124}\mathrm{Sn} + {}^{64}\mathrm{Ni}$ (solid points) reactions. The grey areas are the results of the fit according to Eqs. (8) and (9) (see text).

expected that these values vary also with the source size, and depend on the assumed type of emission (primary or sequential) [99]. This is the reason why it was expected to obtain different values of α and β by changing the reaction partners.

Similarly as in Refs. [26,27], also in our analysis the values of $\hat{\rho_n}$, extracted from isotope ratios and the values of the free neutron-to-proton density ratios for both studied reactions, $(\rho_n/\rho_p)_{124}$ and $(\rho_n/\rho_p)_{112}$, occur much larger than expected for neutrons and protons being homogeneously mixed at the break-up configuration.

For example, assuming that the relative concentrations of neutrons and protons are proportional to the number of nucleons (assuming the same volume for both systems), the relative free neutron densities should be $\hat{\rho_n} = 1.08$ and $\hat{\rho_p} = 0.90$, i.e., much different from the values extracted from the fit. The observed increase of $\hat{\rho_n}$ may indicate a neutron enrichment in the gas phase, while the decrease of $\hat{\rho_p}$ suggests proton depletion, a consequence of n-enrichment in the nucleon gas.

In addition, the free neutron-to-proton density ratios for both studied reactions, $(\rho_n/\rho_p)_{124}$ and $(\rho_n/\rho_p)_{112}$, are larger than the initial N/Z values for both systems, 1.41 and 1.18, respectively. The change in the N/Z values of the two systems is about 20%, while the changes of the mirror-nuclei ratios are about a factor of 2, i.e., much larger than one would expect if the extra neutrons of the neutron-rich system were distributed homogeneously.

The estimated above neutron-to-proton density ratios appear to be too large and difficult to account for within a realistic reaction scenario. In particular, the fact of neglecting the sequential decay in Eq. (9) may not be justified and should be carefully tested. The trend of the obtained results is, however, fully consistent with the isospin distillation effect, a signal predicted for the liquid–gas transition in asymmetric nuclear systems.

7. Conclusions

In summary, we have shown in this paper that for $^{124}Sn + ^{64}Ni$ and $^{112}Sn + ^{58}Ni$ collisions at 35 A MeV, the technique based on the multidimensional analysis (principal component analysis) allowed us to carefully select the most central collisions.

It appears from the comparison with statistical model calculations that the selected multifragmentation events originate from nearly equilibrated source of the same charge, excitation energy and volume. The analysis of isotopically resolved fragments has been presented, showing that the temperatures, evaluated for two reactions from double-isotopic ratios, are in the range typical for reaction processes near the onset of multi-fragment emission. The isotopic temperatures, within errors, were found equal for both studied reactions.

We performed an isoscaling analysis using ratios of the isotopic yields, measured in both studied reactions. The relative neutron and proton densities have been deduced. The observed increase of the relative neutron density is consistent with neutron enrichment in the gas phase. The free neutron-to-proton density ratios for both systems have been obtained from isobar ratios for mirror nuclei. Their values are much larger than expected if neutrons and protons were homogeneously mixed at the break-up configuration.

Our results are consistent with the effect of isospin distillation, a signal predicted in the liquid–gas phase transition. However, more careful studies of the role of sequential decay are required, before claiming that a signature of the phase transition had been experimentally observed in the analyzed reactions.

Acknowledgements

The authors wish to thank R. Bassini, C. Boiano, C. Cali', V. Campagna, R. Cavaletti, O. Conti, E. Costa, M. D'Andrea, A. Distefano, F. Ferrera, F. Fichera, N. Giudice, A. Grimaldi, N. Guardone, S. Hong, P. Litrico, C. Marchetta, S. Marino, D. Moisa, D. Nicotra, G. Peirong, C. Rapicavoli, G. Rizza, G. Sacca', S. Salomone and S. Urso for the technical support during the experiment.

Thanks are due to the Laboratori Nazionali del Sud Tandem and Cyclotron Staff and to L. Calabretta and D. Rifuggiato for having provided beams of very good timing quality.

The authors are also grateful to A. Botvina for the availability of SMM predictions.

One of the authors (E.G.) would like to thank J.B. Natowitz and S. Shlomo for constructive and stimulating discussions.

This work has been partially supported by Grants of Alma Mater Studiorum (Bologna University).

References

[1] B.-A. Li, W. Udo Schröder (Eds.), Isospin Physics in Heavy-Ion Collisions at Intermediate Energies, Nova Science, New York, 2001.
[2] B.-A. Li, Phys. Rev. Lett. 85 (2000) 4221.
[3] L. Scalone, M. Colonna, M. Di Toro, Phys. Lett. B 461 (1999) 9.

[4] V. Baran, M. Colonna, M. Di Toro, A.B. Larionov, Nucl. Phys. A 632 (1998) 287.
[5] V. Baran, M. Colonna, M. Di Toro, V. Greco, M. Zielinska-Pfabé, H.H. Wolter, Nucl. Phys. A 703 (2002) 603.
[6] W.A. Friedman, Phys. Rev. C 42 (1990) 667.
[7] J. Bondorf, A.S. Botvina, A.S. Iljinov, I.N. Mishustin, K. Sneppen, Phys. Rep. 257 (1995) 133.
[8] D.H.E. Gross, Phys. Rep. 279 (1997) 119.
[9] A. Guarnera, et al., Phys. Lett. B 403 (1997) 191.
[10] H. Feldmeier, Nucl. Phys. A 515 (1990) 147;
A. Ono, H. Horiuchi, Phys. Rev. C 53 (1996) 2958.
[11] See, for instance:
U. Lynen, et al., Gesellschaft für Schwerionenforschung Report n. GSI-02-89;
R.T. de Souza, et al., Nucl. Instrum. Methods A 295 (1990) 109;
I. Iori, et al., Nucl. Instrum. Methods A 325 (1993) 458;
J. Pouthas, et al., Nucl. Instrum. Methods A 357 (1995) 418.
[12] A. Pagano, et al., in: M. Ishihara, T. Fukuda, C. Signori (Eds.), Perspectives in Heavy Ion Physics, 2nd Japan–Italy Joint Symposium '95, Riken, Japan, May 22–26, 1995, World Scientific, Singapore, 1995, p. 119;
S. Aiello, et al., Nucl. Phys. A 583 (1995) 461;
S. Aiello, et al., Nucl. Instrum. Methods A 369 (1996) 50;
S. Aiello, et al., Nucl. Instrum. Methods A 400 (1997) 469;
S. Aiello, et al., IEEE Trans. Nucl. Sci. 47 (2) (2000) 114;
F. Porto, et al., Acta Phys. Pol. B 31 (2000) 1489.
[13] M. D'Agostino, et al., Phys. Lett. B 371 (1996) 175.
[14] A.S. Botvina, et al., Nucl. Phys. A 584 (1995) 737.
[15] N. Marie, INDRA Collaboration, Phys. Lett. B 391 (1997) 15.
[16] M.F. Rivet, INDRA Collaboration, Phys. Lett. B 430 (1998) 217.
[17] J.D. Frankland, INDRA Collaboration, Nucl. Phys. A 689 (2001) 940.
[18] N. Bellaize, INDRA Collaboration, Nucl. Phys. A 709 (2002) 367.
[19] D.R. Bowman, et al., Phys. Rev. Lett. 70 (1993) 3534.
[20] T.C. Sangster, et al., Phys. Rev. C 51 (1995) 1280.
[21] E. Cornell, et al., Phys. Rev. Lett. 75 (1995) 1475.
[22] R. Popescu, et al., Phys. Rev. C 58 (1998) 270.
[23] L. Beaulieu, et al., Phys. Rev. Lett. 84 (2000) 5971.
[24] P. Chomaz, Nucl. Phys. A 685 (2001) 274;
P. Chomaz, Proceedings of INPC2001, AIP Proceedings 610 (2002) 167;
B. Borderie, J. Phys G: Nucl. Part. Phys. 28 (2002) R217–R247.
[25] J.B. Natowitz, et al., Phys. Rev. C 65 (2002) 034618;
J.B. Natowitz, et al., Phys. Rev. C 66 (2002) 031601(R);
J.B. Natowitz, et al., Phys. Rev. Lett. 89 (2002) 212701;
J.B. Natowitz, et al., nucl-ex/0206010.
[26] H.S. Xu, et al., Phys. Rev. Lett. 85 (2000) 716.
[27] M.B. Tsang, W.A. Friedman, C.K. Gelbke, W.G. Lynch, G. Verde, H.S. Xu, Phys. Rev. Lett. 86 (2001) 5023.
[28] A.S. Botvina, O.V. Lozhkin, W. Trautmann, Phys. Rev. C 65 (2002) 044610.
[29] C. Schwartz, et al., Preprint GSI-2000-43, November 2000, and nucl-ex/0009003.
[30] G. Verde, et al., Phys. Rev. C 67 (2003) 034606.
[31] R. Ghetti, et al., Phys. Rev. Lett. 91 (2003) 092701.
[32] W.P. Tan, S.R. Souza, R.J. Charity, R. Donangelo, W.G. Lynch, M.B. Tsang, Phys. Rev. C 68 (2003) 034609.
[33] A. Pagano, et al., Nucl. Phys. A 681 (2001) 331.
[34] E. Geraci, REVERSE Collaboration, in: Structure of the Nucleus at the Dawn of the Century, Proceedings of Bologna 2000, Bologna, May 29–June 3, 2000, in: G. Bonsignori, M. Bruno, A. Ventura, D. Vretenar (Eds.), Nucleus–Nucleus Collisions, World Scientific, Sinpapore, 2000, p. 409;
G. Politi, REVERSE Collaboration, in: Structure of the Nucleus at the Dawn of the Century, Proceedings of Bologna 2000, Bologna, May 29–June 3, 2000, in: G. Bonsignori, M. Bruno, A. Ventura, D. Vretenar (Eds.), Nucleus–Nucleus Collisions, World Scientific, Sinpapore, 2000, p. 413.

[35] M. Alderighi, et al., INFN-LNS Activity Report (2000) 96;
M. Alderighi, et al., INFN-LNS Activity Report (2000) 100;
M. Alderighi, et al., IEEE Trans. Nucl. Sci. 48 (2001) 385–390;
M. Alderighi, et al., Comput. Phys. Commun. 140 (2001) 13–20;
M. Alderighi, et al., IEEE Trans. Nucl. Sci. 49 (2002) 1661.
[36] M. Alderighi, et al., Nucl. Instrum. Methods A 489 (2002) 257.
[37] N. Le Neindre, et al., Nucl. Instrum. Methods A 490 (2002) 251.
[38] M. Belkacem, V. Latora, A. Bonasera, Phys. Rev. C 52 (1995) 271.
[39] R.J. Lenk, T.J. Schlagel, V.R. Pandharipande, Phys. Rev. C 42 (1990) 372.
[40] L. Wilet, et al., Nucl. Phys. A 282 (1977) 341.
[41] P.F. Mastinu, et al., Phys. Rev. Lett. 76 (1996) 2646;
A. Bonasera, M. Bruno, C.O. Dorso, P.F. Mastinu, Riv. Nuovo Cimento 23 (2000) 1.
[42] V. Latora, A. Del Zoppo, A. Bonasera, Nucl. Phys. A 572 (1994) 477.
[43] P. Désesquelles, et al., Nucl. Phys. A 633 (1998) 547.
[44] N. Le Neindre, INDRA Collaboration, in: I. Iori, A. Moroni (Eds.), XXXVIII Winter Meeting on Nuclear Physics, Bormio (Italy), 2000, p. 404.
[45] P.M. Milazzo, et al., Phys. Rev. C 58 (1998) 953.
[46] J. Cugnon, D. L'Hôte, Nucl. Phys. A 397 (1983) 519.
[47] R. Bougault, et al., Nucl. Phys. A 488 (1998) 255c.
[48] L. Phair, et al., Nucl. Phys. A 548 (1992) 489.
[49] J. Lukasik, et al., Phys. Rev. C 55 (1997) 1906.
[50] M. D'Agostino, et al., Nucl. Phys. A 650 (1999) 329.
[51] P. Kreutz, et al., Nucl. Phys. A 556 (1993) 672.
[52] A. Schttauf, et al., Nucl. Phys. A 607 (1996) 457.
[53] W. Reisdorf, et al., Nucl. Phys. A 612 (1997) 493.
[54] W. Reisdorf, H.G. Ritter, Annu. Rev. Nucl. Part. Sci. 47 (1997) 553.
[55] T. Li, et al., Phys. Rev. Lett. 70 (1993) 1924.
[56] E. Lloyd, Statistics, Part B, in: Handbook of Applicable Mathematics, vol. VI, Wiley, New York, 1984.
[57] P. Désesquelles, Ann. Phys. (Paris) 20 (1995) 1.
[58] P. Désesquelles, INDRA Collaboration, Phys. Rev. C 62 (2000) 024614.
[59] G.J. Kunde, et al., Phys. Rev. Lett. 77 (1996) 2897.
[60] T.X. Li, et al., nucl-ex/0210004.
[61] A. Grewe, et al., Nucl. Phys. A 614 (1997) 400.
[62] M. de Jong, et al., Nucl. Phys. A 616 (1997) 363c.
[63] C.N. Knott, et al., Phys. Rev. C 53 (1996) 347.
[64] Sl. Cavallaro, et al., Phys. Rev. C 57 (1998) 731.
[65] M. Papa, et al., Proceedings of IWM2001, Catania, December 2001, p. 150;
E. De Filippo, et al., Proceedings of IWM2001, Catania, December 2001, p. 165.
[66] F. Gramegna, et al., Fizika B 12 (2003) 39.
[67] E. Winchester, et al., Phys. Rev. C 63 (2001) 014601.
[68] J. Pochodzalla, W. Trautmann, in: B.-A. Li, W.U. Schröder (Eds.), Isospin Physics in Heavy-Ion Collisions at Intermediate Energies, Nova Science, New York, 2001, p. 451.
[69] R. Wada, et al., Phys. Rev. Lett. 58 (1987) 1829;
H.W. Barz, H. Schulz, J.P. Bondorf, J. Lopez, K. Sneppen, Phys. Lett. B 211 (1988) 10;
E. Ramakrishnan, et al., Phys. Rev. C 57 (1998) 1803.
[70] E. Geraci, Reverse Collaboration, Report LNS 22-05-01 (2001);
S. Pirrone, Reverse Collaboration, in: G. Fazio, G. Giardina, F. Hanappe, G. Immè, N. Rowley (Eds.), Nuclear Physics at Border Lines, Proc. of Int. Conf., Lipari, May 21–24, 2001, World Scientific, Singapore, 2002, p. 267.
[71] M. Papa, T. Maruyama, A. Bonasera, Phys. Rev. C 64 (2001) 024612;
M. Papa, A. Bonasera, G. Cardella, T. Maruyama, Heavy Ion Phys. 16 (1–4) (2002) 223;
M. Papa, A. Bonasera, T. Maruyama, 4th Catania Relativistic Ion Studies Cris 2002, AIP Conf. Proc. 644 (2002).
[72] M. Colonna, N. Colonna, A. Bonasera, M. Di Toro, Nucl. Phys. 541 (1992) 295.

[73] J. Lukasik, Z. Majka, Acta Phys. Pol. B 24 (1993) 1959.
[74] M. Colonna, Ph. Chomaz, Phys. Rev. C 49 (1994) 1908.
[75] R. Hanbury-Brown, R.Q. Twiss, Nature 178 (1956) 1046.
[76] D. Fox, et al., Phys. Rev. C 47 (1993) R421.
[77] T. Glasmacher, et al., Phys. Rev. C 50 (1994) 952.
[78] Y.D. Kim, et al., Phys. Rev. C 45 (1992) 338;
Y.D. Kim, et al., Phys. Rev. C 45 (1992) 387.
[79] R. Trockel, et al., Phys. Rev. Lett. 59 (1987) 2844.
[80] E. Cornell, et al., Phys. Rev. Lett. 77 (1996) 4508.
[81] E. Geraci, in preparation.
[82] N. Marie, INDRA Collaboration, Phys. Rev. C 58 (1998) 256;
S. Hudan, INDRA Collaboration, Phys. Rev. C 67 (2003) 064613.
[83] S. Albergo, S. Costa, E. Costanzo, A. Rubbino, Nuovo Cimento A 89 (1985) 1.
[84] S. Albergo, S. Costa, S. Pirrone, A. Rubbino, Nuovo Cimento A 101 (1989) 815.
[85] A. Kolomiets, et al., Phys. Rev. C 54 (1996) R472;
A. Kolomiets, et al., Phys. Rev. C 55 (1997) 1376.
[86] M.B. Tsang, W.G. Lynch, H. Xi, W.A. Friedman, Phys. Rev. Lett. 78 (1997) 3836.
[87] J. Pochodzalla, et al., Phys. Rev. Lett. 75 (1995) 1040.
[88] K. Kwiatkowski, et al., Phys. Lett. B 423 (1998) 21.
[89] J.A. Hauger, et al., Phys. Rev. C 62 (2000) 024616.
[90] H. Muller, B.D. Serot, Phys. Rev. C 52 (1995) 2072.
[91] B.-A. Li, C.M. Ko, Nucl. Phys. A 618 (1997) 498.
[92] Ph. Chomaz, F. Gulminelli, Phys. Lett. B 447 (1999) 221.
[93] S.K. Samaddar, S. Das Gupta, Phys. Rev. C 61 (2000) 34610.
[94] V. Baran, M. Colonna, M. Di Toro, V. Greco, Phys. Rev. Lett. 86 (2001) 4492;
M. Colonna, Ph. Chomaz, S. Ayik, Phys. Rev. Lett. 88 (2002) 122701.
[95] Y.G. Ma, et al., Phys. Rev. C 60 (1999) 24607.
[96] G.J. Kunde, et al., Phys. Lett. B 416 (1998) 56.
[97] J. Randrup, S.E. Koonin, Nucl. Phys. A 356 (1981) 223.
[98] M.B. Tsang, et al., Phys. Rev. C 64 (2001) 054615.
[99] S.R. Souza, et al., Phys. Rev. C 67 (2003) 051602R.